interatomic vector positions. Table 1 shows that the typical deviation between observed and correct vector positions is $\sim 0.0015a = 0.007$ Å, a full order of magnitude less than the pixel resolution ($a/60 \simeq 0.08$ Å) and almost two orders of magnitude less than the minimum d spacing measured (0.487 Å). The oxygen fractional coordinate calculated from the maximum-entropy Patterson map is 0.3047, essentially identical to the correct value of 0.3048. Moreover, the intensities of these interatomic vectors are in good agreement with expected values (Table 1) and there is even some evidence of the anisotropy of the thermal motion of the oxygen atoms (Fig. 2f). The algorithm has produced an optimally sharpened Patterson map and thus opens up a productive route for the solution of crystal structures.

Evaluation of the individual squared magnitudes of the structure factor was performed by back-transformation of the maximum-entropy Patterson map (for a full list of structure factors see Supplementary Information). A comparison of the following R factors shows that there is a clear superiority in the $|F(\mathbf{h})|^2$ derived from the maximum-entropy algorithm over the a priori equipartioned values.

$$R_{EQ} = \left[\sum_{}^{N_F} w(\mathbf{h})(F(\mathbf{h})_{EQ} - F(\mathbf{h}))^2 / \sum_{}^{N_F} w(\mathbf{h})F(\mathbf{h})^2 \right]^{1/2} = 34.0\%$$

$$R_{ME} = \left[\sum_{}^{N_F} w(\mathbf{h})(F(\mathbf{h})_{ME} - F(\mathbf{h}))^2 / \sum_{}^{N_F} w(\mathbf{h})F(\mathbf{h})^2 \right]^{1/2} = 14.1\%$$

$$R_{EX} = \left[N_F / \sum_{}^{N_F} w(\mathbf{h})F(\mathbf{h})^2 \right]^{1/2} = 6.5\%$$

R_{EQ} and R_{ME} are the R factors for the $|F(\mathbf{h})|$ obtained from the refinement of the Pawley profile and from the maximum-entropy algorithm, respectively, and R_{EX} is the expected R factor based on statistical errors. N_F is the number of different $|F(\mathbf{h})|$ and $w(\mathbf{h})$ is the inverse square oi the estimated standard deviation of $|F(\mathbf{h})|$. Moreover, for all clumps of reflections the method correctly discriminates between strong and weak intensities, albeit usually with a slightly reduced contrast than for the true values. Indeed, the $|F(\mathbf{h})|^2$ derived from the maximum-entropy algorithm for intensity clumps containing up to five reflections agree well with true values even at short d spacings close to the limits of the diffraction data. A further indication of the success with which the maximum-entropy algorithm has optimally combined the intensity information is provided by consideration of the sign of $|F(\mathbf{h})|^2$. Although the
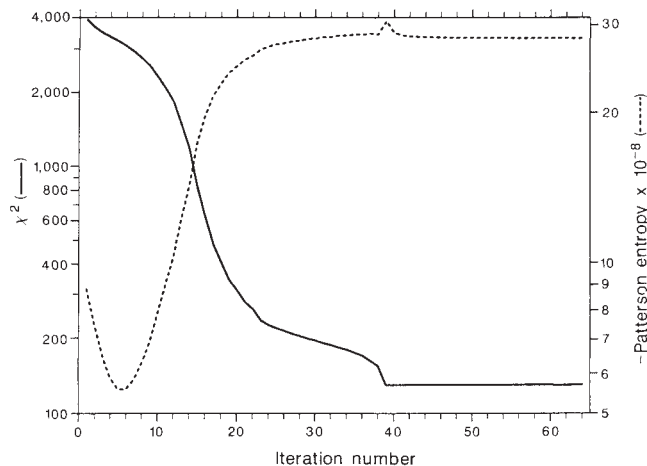
least-squares profile refinement has yielded negative values for some $|F(\mathbf{h})|^2$, all 177 $|F(\mathbf{h})|^2$ obtained by back-transformation of the maximum-entropy Patterson map are positive quantities. In general, therefore, the $|F(\mathbf{h})|^2$ obtained by the maximum-entropy method can be used to increase the potential for success of a direct-methods approach to structure solution using powder data.

It is worth considering two broader implications of the maximum-entropy formalism that may have important ramifications for ab initio structure solution. The Patterson maps produced may be regarded as being optimally sharpened and thus be the closest approach to a true interatomic vector map. Although computationally expensive, this has broad implications for Patterson methods and will assist in the current revival[8] of the technique as an important alternative to direct methods of structure solution[9,10]. Furthermore, the formalism uses the information content contained in negative scattering factors. Many aspects of direct methods of structure solution from X-ray data rely implicitly on the inherent positivity of the electron scattering density. This poses concerns for neutron diffraction data where the scattering density may be both positive and negative and, indeed, weakens the power of direct methods in such situations. Here, the negative scattering density is a bonus. Consider, for example, a molecule in an asymmetric unit of a unit cell and containing a single atom with a negative scattering length. The negative peaks in the maximum-entropy Patterson map only correspond to vectors between the negative scatterer and all the other atoms. Such a situation bears a close resemblance to isomorphous replacement[11,12] and anomalous dipersion[12] methods. Examination of the negative Patterson features uniquely defines the location and orientation of the molecule with respect to the negatively scattering atom. □

1. Rietveld, H. M. J. appl. Crystallogr. **2**, 65–71 (1969).
2. David, W. I. F. J. appl. Crystallogr. **20**, 316–319 (1987).
3. Gull, S. F. & Daniell, G. J. Nature **272**, 686–690 (1978).
4. Livesey, A. K. & Skilling, J. Acta Crystallogr. A**41**, 113–122 (1985).
5. Bricogne, G. Acta Crystallogr. A**40**, 410–445 (1984).
6. Hull, S. & Mayers, J. User Guide for the Polaris Powder Diffractometer at ISIS, Rep. RAL-89-118 (Rutherford Appleton Laboratory, Chilton, 1989).
7. Pawley, G. S. J. appl. Crystallogr. **14**, 347–361 (1981).
8. Egert, E. Acta Crystallogr. A**39**, 936–940 (1983).
9. Woolfson, M. M. Acta Crystallogr. A**43**, 593–612 (1987).
10. Ladd, M. F. C. & Palmer, R. A. (eds) Theory and Practice of Direct Methods in Crystallography (Plenum, London, 1980).
11. Rossmann, M. G., Arnold, E. & Vriend, G. Acta Crystallogr. A**42**, 325–334 (1986).
12. Karle, J. Acta Crystallogr. A**45**, 765–781 (1989).

FIG. 3 Evolution of the entropy and χ^2 goodness of fit for the construction of the maximum-entropy Patterson map. (The negative value of the Patterson entropy is plotted as it is an intrinsically negative property.) The entropy decreases initially as the Patterson map changes from the flat uniform distribution to one consistent with the observed data ($\chi^2 = 130$) after 39 iterations. Once agreement with the observed diffraction intensities has been obtained the entropy increases to its maximum value consistent with the χ^2 constraint.

Sensitivity of regional climates to localized precipitation in global models

A. J. Pitman, A. Henderson-Sellers & Z-L. Yang

School of Earth Sciences, Macquarie University, North Ryde, NSW 2109, Australia

ATMOSPHERIC general circulation climate models are valuable tools for investigating the effects that large-scale perturbations (for example, increasing greenhouse gases[1], volcanic dust in the atmosphere[2], deforestation[3,4] and desertification[5]) might have on climate. Designed for global-scale climate simulations and having coarse spatial resolutions (from ~ 250 km (ref. 6) to 800 km (ref. 7)) such models are now being used to evaluate climatological and hydrological quantities at or near the land surface and at sub-continental scales[8–10]. They are also being used to provide input data for high-resolution simulations, predicting, for example, the

effects of increasing atmospheric CO_2 at regional scales[11]. Here we show that continental surface climatologies and climate change predictions for tropical forest ecotypes derived from general circulation models may be very sensitive to slight modifications in the land-surface/atmosphere coupling. Specifically our results indicate that improving the realism of the areal distribution of precipitation alters the balance between runoff and evaporation. In the case of a tropical forest, we find that by modifying the area over which rainfall is distributed, the surface climatology is changed from an evaporation-dominated regime to one dominated by runoff. Climate studies using near-surface output from such simulations may therefore be misleading.

The land surface is an essential component in atmospheric general circulation models (AGCMs). A series of sensitivity experiments[12] has shown that the simulation of the Earth's climate is affected by the land surface[3,8] and its representation[9,13]. In the past decade several models for parameterizing the land surface in AGCMs have been designed[4,14,15]. The latest include detailed soil and canopy models which, under the observed climatological forcing, realistically simulate surface–atmosphere energy fluxes, temperatures and the water balance for specific locations[3,9]. Although these land surface models are realistic, the atmospheric quantities output by the AGCM are not always compatible with those required by the land surface models. For instance, virtually all current AGCMs predict the precipitation rate as a grid-element average, that is, a single value for precipitation is calculated for each grid element at each timestep. Thus both large-scale (such as frontal) and small-scale (such as convective) precipitation is assumed to fall uniformly over the entire grid element. In the case of large-scale precipitation this may be satisfactory (particularly for models with spatial resolutions of $\sim 300 \times 300$ km). In the case of small-scale precipitation, however, this grid-average assumption leads to a loss of physical realism. Specifically, current AGCMs predict drizzle across entire grid areas rather than intense convective precipitation concentrated in much smaller areas within grids. In the former situation a much greater proportion of the rainfall will be intercepted by the vegetation canopy and subsequently re-evaporated, whereas in the latter, more realistic situation, throughfall and hence runoff will be much greater. This modification in the partitioning of precipitation between runoff and evaporation has the potential to affect the energy and hydrological balance of the land surface. It may also cause systematic changes in the predictions by AGCMs once feedbacks are incorporated. These effects will be most pronounced in regions where dense vegetation exists and where convective precipitation is common, for example, in tropical forest areas.

Tropical convective precipitation can produce point-measured precipitation intensities of 10 mm h^{-1} but the spatial extent of such storms is only ~ 100 km^2. At this intensity, a canopy would saturate rapidly leading to leaf drip and therefore a large proportion of the precipitation would reach the soil surface where it would either infiltrate or run off. In an AGCM, convective precipitation is spread over the entire grid element. Assuming grid areas of 100,000 km^2 ($\sim 3° \times 3°$) and a precipitation intensity of 10 mm h^{-1} leads to a precipitation intensity over the entire grid element of $\sim 10^{-2}$ mm h^{-1}. In this case the canopy would intercept and retain virtually all the precipitation, contrary to observation.

The evaporation of precipitation intercepted by a canopy occurs very rapidly in comparison to the evaporation of water that infiltrates the soil surface. The low precipitation intensities 'predicted' by AGCMs could therefore lead to fundamentally misleading hydrological simulations because precipitation recycling from the surface to the atmosphere, in any AGCM incorporating a vegetation canopy, will be overestimated at the expense of increasing soil moisture or runoff. To overcome this problem it is important to account for both the spatial extent and intensity of precipitation in AGCMs that incorporate the new generation of land surface schemes.

Here we investigate, using the Biosphere–Atmosphere Transfer Scheme (BATS)[15], a method of retaining the spatial extent and intensity of precipitation for AGCMs suggested elsewhere[16,17]. Throughout this discussion water fluxes are in units of kg m^{-2} s^{-1} (1 kg m^{-2} s^{-1} = 1 mm s^{-1}). It is possible to derive an expression for surface runoff[16] R_{surf} and canopy drip[17] R_{drip} by assuming that the local precipitation rate (over a fraction μ of the grid element) is described by a decaying exponential probability distribution. We note that although subgridscale variations exist in R_{surf} and R_{drip} within a timestep, knowledge of the distribution of local precipitation is not propagated—at the end of a timestep the soil moisture and intercepted water are assumed to be distributed uniformly within the grid element. This is clearly inconsistent with the definition of the net flux of water at the surface, P_s, but no method yet exists to account for subgridscale variations in intercepted water and soil moisture in AGCMs. Expressions for R_{surf} and R_{drip} are given by

$$R_{surf} = P_s \exp\left(\frac{-\mu F_s}{P_s}\right) \qquad (1)$$

where F_s is the maximum surface infiltration rate, assumed constant over the grid element. Similarly, the canopy drip rate is

$$R_{drip} = P_c \exp\left(\frac{-\mu F_c}{P_c}\right) \qquad (2)$$

where P_c is the precipitation intercepted by the canopy and F_c is the maximum canopy infiltration rate, assumed constant over the grid element. F_c is defined as the difference between the canopy storage capacity and the water stored on the canopy, divided by the model timestep.

In the standard version of BATS, R_{surf} is given by

$$R_{surf} = \beta^4 P_s \qquad (3)$$

where β is a depth-weighted ratio of the soil wetness. Equation (3) predicts $R_{surf} > 0$ when any water falls to the surface. The canopy drip is usually determined by the storage capacity S (kg m^{-2}). In a timestep Δt when the mass of intercepted water per unit leaf area C (kg m^{-2}) on the canopy exceeds S, all water in excess of S falls to the surface

$$R_{drip} = (C - S)/\Delta t \qquad (4)$$

Here we replace these standard formulae by equations (1) and (2).

Using the modified version of BATS in a stand-alone mode[10] (that is, uncoupled from the GCM), and prescribing atmospheric forcing (including precipitation, air temperature, solar radiation, downward near-infrared radiation and wind speed) with seasonal and diurnal cycles from climatological estimates[18], the model was integrated for a two-year simulation to investigate the sensitivity of the land surface to changes in the definition of μ. Here we report results of the second year of integration (these results are independent of initial conditions) for a tropical forest, with μ set to 1.0 (rainfall over the whole grid element), 0.5 and 0.1. The results from the control simulation using the standard version of BATS are also included. We consider tropical forest and tropical rainfall because the dense canopy and the high leaf-area index typical of this ecotype leads to a high sensitivity to the type (and here the spatial extent) of precipitation simulated by AGCMs and because of the number of Amazonian deforestation experiments conducted using AGCMs[3,4,19]. These results are, however, likely to be appropriate to all regions where precipitation falls at spatial scales less than the resolution of the AGCM.

Figure 1 shows four sets of histograms of precipitation, evaporation and runoff for the four simulations. In each case the monthly total precipitation is identical, as is the atmospheric forcing but the fraction of the grid square over which the precipitation is prescribed to fall is variable.

The control simulation using the standard BATS model (Fig. 1a) shows that the seasonal variation in evaporation is limited,
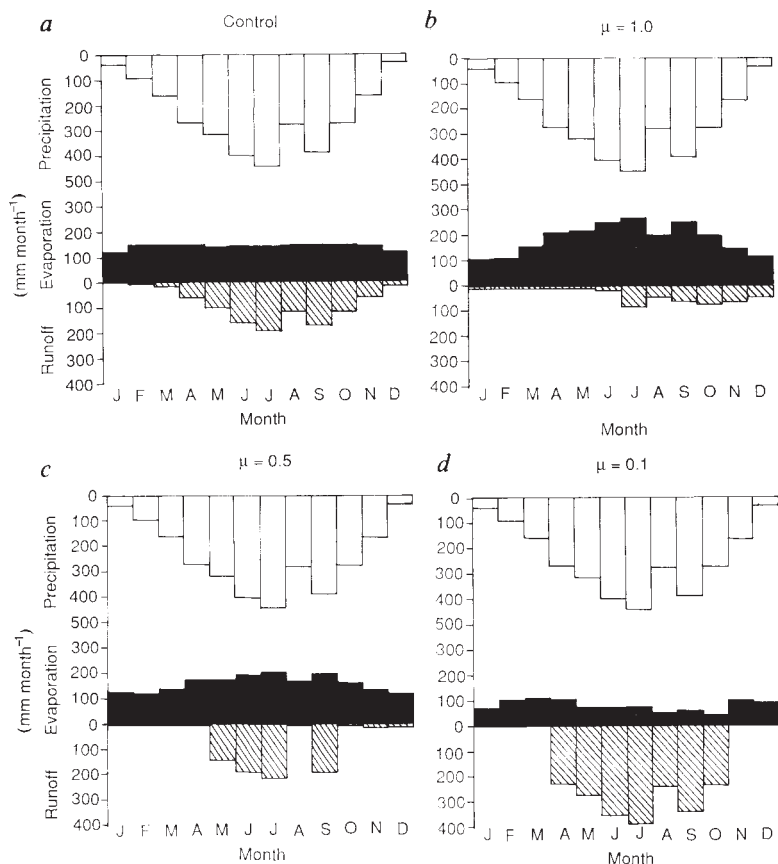
FIG. 1 Results from the second year of four 2-yr stand-alone simulations showing the seasonal variation in the precipitation (open bars), evaporation rates (solid bars) and runoff (hatched bars) for a, the control simulation (standard BATS without the μ-parameterization), b, BATS plus the μ-parameterization with $\mu = 1.0$; c, $\mu = 0.5$; d, $\mu = 0.1$. The precipitation forcing varies from 34 mm month^{-1} in December to 440 mm month^{-1} in July. The air temperature varies seasonally and diurnally, with the annual maximum in March–April (301 K) and the minimum in July–August (298 K) and a diurnal temperature range of 3 K. The wind velocity (at the height of the canopy) is constant at 3 m s^{-1} and the atmospheric pressure is constant at 1,000 hPa. Solar radiation varies seasonally and diurnally and is reduced after rainfall in an attempt to simulation the gross effects of cloud cover.

with the precipitation in excess of evaporation during the summer months (JJA) forming runoff. BATS incorporating the μ-parameterization (replacing equations (3) and (4) by equations (1) and (2)) produces very different simulations. Figure 1b ($\mu = 1.0$) shows much higher evaporation fluxes and very little runoff. For $\mu = 1.0$, the precipitation is distributed over the entire grid square leading to relatively low intensities. The dense canopy of the tropical forest intercepts much of the rainfall leading to higher monthly evaporation, but much lower runoff rates.

Although the spatial extent of precipitation in Fig. 1a, b is the same (distributed over the entire grid element, although non-uniform in Fig. 1b) it is clear that the resulting simulation of evaporation and runoff is quite different because the actual formulations of R_{surf} and R_{drip} are different. This leads to a change in the amount of precipitation that is intercepted and evaporated or that reaches the soil surface. The differences between Fig. 1a, b show how sensitive the simulation of the partitioning of precipitation between runoff and evaporation is to minor changes in the formulation of the land surface in AGCMs.

As μ is reduced from 1.0, the effective precipitation intensity is increased and interception rates are reduced, leading to lower evaporation and higher runoff. Figure 1c shows the case for $\mu = 0.5$. Evaporation shows some dependence on season (although less than in Fig. 1b) and high runoff during the summer months. Figure 1c shows negligible runoff in April, October and November, however, in contrast to Fig. 1a. Finally, Fig. 1d shows the simulation for $\mu = 0.1$. Here, precipitation is concentrated over 10% of the grid element, hence its effective intensity is relatively high. Figure 1d shows that there is relatively little evaporation except in February, March, April, November and December when evaporation rates are comparable with the minimum rates in Fig. 1a–c. The runoff simulated with $\mu = 0.1$ is dramatically higher than in the previous simulations. The high precipitation intensities lead to very low interception and high runoff rates for seven months of the year. In this case the canopy

becomes saturated rapidly in a precipitation event, leading to high throughfall and subsequently large runoff rates.

The change from Fig. 1a or Fig. 1b to Fig. 1d is somewhat similar (decreased evaporation and increased runoff) to modelled results of tropical deforestation[3] although the only disturbance is in the spatial distribution of a constant precipitation amount falling on unchanged tropical forest. This implies that recent estimates of the impact on climate of tropical deforestation[3,4,19] are inconsistent because two[4,19] include some description of subgridscale precipitation and two[3,19] include a canopy parameterization. It is probably unrealistic simply to incorporate a μ-parameterization without considering very carefully the likely impact on the hydrology, which is a function of the canopy scheme. The relative and combined importance of subgridscale precipitation and vegetation must be more thoroughly investigated.

The quantitative values in the histograms of runoff and evaporation in Fig. 1 are of less importance (because minor changes in the land surface parameterization or in the prescribed atmospheric forcing would alter magnitudes) than the relative shapes of the seasonal distributions. The differences in the seasonal distributions shown in Fig. 1a–d are of considerable importance to potential users of AGCM simulations for quantities at or near the land surface. Figure 1 shows clearly that the surface hydrological climatology is highly sensitive to atmospheric 'forcing', in this case precipitation. Simply by changing the area over which precipitation is distributed, the surface climatology can be changed from an evaporation-dominated regime (Fig. 1b) to one dominated by runoff (Fig. 1d).

By prescribing atmospheric forcing, feedback effects between the surface and the atmosphere are prevented. As it is not obvious what direction feedbacks would take, it is unclear whether the simulations presented here are amplifications of the fully interactive result, or whether the results are damped. It is therefore necessary to analyse the μ-type parameterization in an AGCM before developing the methodology further.

These simulations suggest that it may not be possible to

736

improve the simulation of climate at the land surface by improving only the land surface models. Advances in land surface modelling must be made in tandem with improvements in the coupling between the land surface and atmosphere. The addition of vegetation and soil processes to AGCMs improves physical realism, but it also has the potential to increase the sensitivity of the surface to the atmosphere. If incorporation of these more complete land surface submodels is considered desirable then the simulation of precipitation, including its subgridscale variability, must be improved. We do not necessarily claim improved accuracy for any of the regimes illustrated in Fig. 1, because observational evidence is not yet sufficiently accurate to validate any particular simulation. Rather we point out that including the effects of spatial heterogeneity in precipitation increases the physical realism of the model simulations and therefore its consequences must be fully investigated.

The distribution of precipitation within grid elements needs to be incorporated into the AGCMs that include vegetation. Its calculation is fairly straightforward[20] but even specifying precipitation intensities of large-scale and small-scale precipitation events as different but constant values[16,17] would improve the simulation of near-surface quantities. This approach is dangerous, however, because a constant value for μ could lead to a climatology dependent on the value chosen for μ. Figure 1a-d implies that using AGCM simulations of near-surface variables from models that incorporate a parameterization of vegetation, but do not consider subgridscale variability of

precipitation, are misleading. Our results indicate that using results of AGCMs for regional-scale impact studies of, for example, greenhouse warming or deforestation might be very misleading unless the limitations of the model are clearly understood. □

1. Mitchell, J. F. B., Wilson, C. A. & Cunnington, W. M. Q. Jl R. met. Soc. 113, 293–322 (1987).
2. Hansen, J. et al. Science 213, 957–966 (1981).
3. Dickinson, R. E. & Henderson-Sellers, A. Q. Jl R. met. Soc. 114, 439–462 (1988).
4. Lean, J. & Warrilow, D. A. Nature 342, 411–413 (1989).
5. Charney, J., Quirk, W. J., Chow, S-H. & Kornfield, J. J. atmos. Sci. 34, 1366–1385 (1977).
6. Rowntree, P. R. & Bolton, J. A. Q. Jl R. met. Soc. 109, 501–526 (1983).
7. Hansen, J. E. et al. Mon. Wea. Rev. 111, 609–662 (1983).
8. Rind, D. J. geophys. Res. 93, 5385–5412 (1988).
9. Sato, N. et al. NASA Contractor, Rep. 185509 (NASA, Washington, DC, 1989).
10. Wilson, M. F., Henderson-Sellers, A., Dickinson, R. E. & Kennedy, P. J. J. Clim. appl. Met. 26, 341–362 (1987).
11. Cohen, S. J. & Allsopp, T. R. J. Clim. 1, 669–681 (1988).
12. Mintz, Y. in The Global Climate (ed. Houghton, J. T.) 79–105 (Cambridge University Press, 1984).
13. Mitchell, J. F. B. & Warrilow, D. A. Nature 330, 238–240 (1987).
14. Sellers, P. J., Mintz, Y., Sud, Y. C. & Dalcher, A. J. atmos. Sci. 43, 505–531 (1986).
15. Dickinson, R. E., Henderson-Sellers, A., Kennedy, P. J. & Wilson, M. F. NCAR Tech. Note, TN275 +STR (Natn. Center for Atmospheric Research, Boulder, 1986).
16. Warrilow, D. A., Sangster, A. B. & Slingo, A. Dynamic Climatology Tech. Note 38 (Meteorological Office, Bracknell, 1986).
17. Shuttleworth, W. J. J. Hydrol. 100, 31–56 (1988).
18. Dickinson, R. E. (ed.) The Geophysiology of Amazonia (Wiley, New York, 1987).
19. Shukla, J., Nobre, C. & Sellers, P. J. Science 247, 1322–1325 (1990).
20. Entekhabi, D. & Eagleson, P. S. J. Clim. 2, 816–831 (1989).

Partly pedogenic origin of magnetic variations in Chinese loess

L. P. Zhou*, F. Oldfield†, A. G. Wintle‡, S. G. Robinson§ & J. T. Wang‖

* Godwin Laboratory, Subdepartment of Quaternary Research, University of Cambridge, Free School Lane, Cambridge CB2 3RS, UK
† Department of Geography, University of Liverpool, PO Box 147, Liverpool L69 3BX, UK
‡ Institute of Earth Studies, University College of Wales, Aberystwyth SY23 3DB, UK
§ Department of Earth Sciences, University of Cambridge, Downing Street, Cambridge CB2 3EQ, UK
‖ Geological Hazards Research Institute, Lanzhou, Gansu, China

QUATERNARY sequences of interbedded aeolian silts (loess) and buried soils (palaeosols) potentially provide one of the best terrestrial records of past climates[1-5]. Magnetic susceptibility variations in loess and palaeosol sequences from China are strongly correlated with climate-induced fluctuations of oxygen isotope ratios in deep-sea sediments[2-4,6-8]. As an explanation of this correlation, it has been suggested that the recorded variations in magnetic susceptibility depend primarily on the degree of dilution by non-magnetic bulk loess constituents of a uniform magnetic assemblage derived from remote but unknown sources[6-8]. It has also been suggested that such a model, involving changes in the accumulation rate of loess superimposed on a constant flux of magnetic particles, provides a relative geological timescale through the control of loess deposition by astronomically modulated climate fluctuations[7]. Here we report a preliminary test of this model using rock magnetic properties especially sensitive to variations in magnetic grain size. Our results show that palaeosols are characterized by much finer magnetic grain size assemblages than are the intervening loess units. This suggests that a simple model based on constant magnetic influx and dilution by variable amounts of non-magnetic loess is inadequate. Our magnetic measurements establish the close comparability of the fine grained magnetic minerals in the

palaeosol samples to those in contemporary soils and thus point to a partially pedogenic origin for the magnetic mineral assemblages in the palaeosols.

Here we present results obtained from two groups of samples. One (Fig. 1) consists of 17 samples of late Pleistocene loess and a palaeosol from Xifeng, Gansu (35.7° N, 107.6° E). The other (Fig. 2a, b) consists of samples taken from eight successive palaeosols and the loess units above and below them in the upper part of a Quaternary loess section near Lanzhou, Gansu (36.1° N, 103.8° E). Magnetic measurements were made on air-dried, disaggregated and weighed subsamples.

Several recent studies describe the instrumentation used for magnetic measurements and outline the way in which they may be interpreted[9-11]. These studies show how rock magnetic measurements, which reflect variations in magnetic mineralogy and grain size, can be used to characterize soils, dusts and sediments, to differentiate them and to establish their origins. Here the results from Xifeng (Fig. 1) are plotted in stratigraphic sequence, whereas those from the Lanzhou section (Fig. 2a, b) are presented as bivariate plots.

Figure 1 shows that field and laboratory measurements of the profile of the magnetic susceptibility are in excellent agreement, and that the latter are only slightly affected by expressing the results on a carbonate-free basis. The magnetic susceptibilities in palaeosol horizons are over three times higher and the χ_{fd} and χ_{ARM} values, which are strongly correlated, generally five to seven times higher than those in the loess. Moreover, variations in the normalized quotients $\chi_{fd}(\%)$ and $\chi_{ARM}/SIRM$ are positively correlated and in $SIRM/\chi$ negatively correlated with those in bulk magnetic susceptibility. These variations must therefore reflect differences between the samples in the relative proportions of different magnetic components, and cannot be caused simply by changes in the degree of dilution by non-magnetic constituents in the samples. More specifically, variations in $\chi_{ARM}/SIRM$ can be explained only in terms of the behaviour of the remanence-carrying minerals and cannot be affected by paramagnetic or diamagnetic components.

Measurements of IRM acquisition (not shown here) confirm that all samples from both sections attain 92–97% of the SIRM in a forward field of 300 mT. Therefore we conclude that the